

WSe₂ as transparent top gate for near-field experiments

Niels C.H. Hesp,¹ Mark Kamper Svendsen,² Kenji Watanabe,³ Takashi Taniguchi,⁴
Kristian Sommer Thygesen,^{2,5} Iacopo Torre,^{1,*} and Frank H.L. Koppens^{1,6,†}

¹ICFO-Institut de Ciències Fotòniques, The Barcelona Institute of Science and Technology,
Av. Carl Friedrich Gauss 3, 08860 Castelldefels (Barcelona), Spain

²CAMD, Computational Atomic-Scale Materials Design, Department of Physics,
Technical University of Denmark, DK - 2800 Kongens Lyngby, Denmark

³Research Center for Functional Materials, National Institute for Materials Science, 1-1 Namiki, Tsukuba 305-0044, Japan

⁴International Center for Materials Nanoarchitectonics,
National Institute for Materials Science, 1-1 Namiki, Tsukuba 305-0044, Japan

⁵Center for Nanostructured Graphene (CNG), Department of Physics,
Technical University of Denmark, DK - 2800 Kongens Lyngby, Denmark

⁶ICREA-Institució Catalana de Recerca i Estudis Avançats, 08010 Barcelona, Spain

Independent control of carrier density and out-of-plane displacement field is essential for accessing novel phenomena in two-dimensional material heterostructures. While this is achieved with independent top and bottom metallic gate electrodes in transport experiments, it remains a challenge for near-field optical studies as the top electrode interferes with the optical path. Here, we systematically characterize the requirements for a material to be used as top-gate electrode, and demonstrate experimentally that few-layer WSe₂ can be used as a transparent, ambipolar top gate electrode in infrared near-field microscopy. We perform nano-imaging of plasmons in a bilayer graphene heterostructure and tune the plasmon wavelength using a trilayer WSe₂ gate, achieving a density modulation amplitude exceeding $2 \cdot 10^{12} \text{ cm}^{-2}$. Moreover, the observed ambipolar gate-voltage response allows to extract the energy gap of WSe₂ yielding a value of 1.05 eV. Our results will provide an additional tuning knob to cryogenic near-field experiments on emerging phenomena in 2d-materials and moiré material heterostructures. Near-field optical microscopy is a powerful technique for exploring the optical properties of materials on the nanoscale¹.

Scattering-type scanning near-field microscopy (s-SNOM) is the most commonly used type of near-field optical microscopy in the study of two-dimensional (2D) materials and their heterostructures. In this configuration a sharp metallic tip (with a typical apex radius of $\approx 20 \text{ nm}$) generates a hotspot of light that interacts with the sample. The tip also bridges the momentum mismatch between free-space light and collective excitations, like plasmon^{2,3} or phonon polaritons^{4,5}, making s-SNOM an appealing tool for imaging these excitations^{6,7}.

Importantly, in 2D materials it is possible to continuously tune the carrier density via the field effect, using a gate electrode underneath the sample. Notably, in single-layer graphene, tuning the carrier density has allowed for understanding of the mechanism of photocurrent generation in near-field photocurrent experiments⁸. Moreover, the carrier density has a direct impact on the plasmon dispersion. Varying the carrier density in s-SNOM experiments on graphene

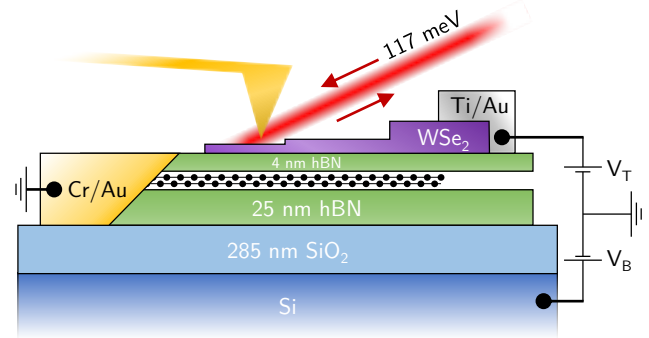


Fig. 1 | Device schematic. Schematic of our near-field experiment performed on a device consisting of hBN-encapsulated bilayer graphene. By applying a voltage to a staircase flake of WSe₂ (2-6 layers), we tune the carrier density in bilayer graphene without obstructing the near-field access, as verified by probing the plasmon properties. Together with the silicon bottom gate this allows full control of the carrier density and displacement field in bilayer graphene.

plasmons^{2,3,9,10} has given crucial information to understand the nature of these collective excitations, and the role of many-body effects¹¹. Tuning the carrier density also gave an insight into the plasmonic properties of a photonic lattice formed by minimally twisted bilayer graphene¹². The modulation of the carrier density can also be exploited to enhance the signal to noise ratio of the recorded signal via a lock-in detection scheme. This technique was employed to detect intersubband transitions in transition metal dichalcogenides (TMDs)¹³. The application of a gate voltage on a sample has an additional consequence: beside injecting carriers into the sample, it induces a perpendicular electric displacement field. Whilst the effect of the displacement field on the properties of single-layer graphene is minor, it can have a more pronounced impact on multilayer materials. For instance, a displacement field leads to an opening of a band gap in bilayer graphene¹⁴. Hence, independent control of the carrier density and displacement field is of great relevance for exploring novel phenomena in 2D materials using s-SNOM. For example, domain walls in gapped bilayer graphene are predicted to host long-lived plasmons with lifetimes two orders of magnitude higher than in single-layer graphene¹⁵. Recent experiments have shown tunability

* iacopo.torre@icfo.eu

† frank.koppens@icfo.eu

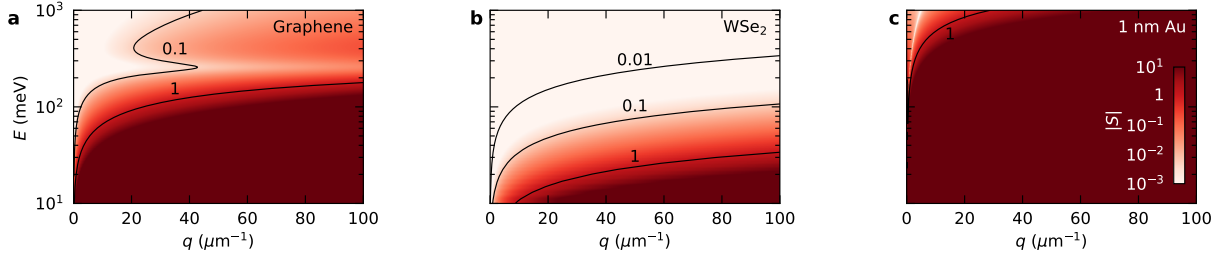


Fig. 2 | Optical disturbance introduced by different top layers. **a.** Calculated $|S|(q, \omega)$ for single-layer graphene with $n = 2 \cdot 10^{12} \text{ cm}^{-2}$, $\tau = 200 \text{ fs}$ at room temperature. The full non-local longitudinal conductivity has been taken into account. The horizontal feature appearing at $\approx 300 \text{ meV}$ is related to the onset of interband transitions at twice the Fermi energy. **b.** Same as **a.** for trilayer WSe_2 , modeled as a Drude conductor with $n = 2 \cdot 10^{12} \text{ cm}^{-2}$, $m^* = 1.2 m_e$, $\tau = 100 \text{ fs}$. **c.** Same as in **a.** for a 1 nm thick gold film. Permittivity of gold is taken from Ref. 28.

of correlated states in twisted double bilayer graphene using a displacement field^{16,17}, while twisted trilayer graphene under a displacement field has raised the bar of the superconductivity critical temperature in graphene-based systems beyond 2 K^{18,19}.

Independent control of carrier density and displacement field is achieved in transport experiments by placing two separately-contacted gate electrodes, one on the top and one on the bottom of the sample. This is more difficult in optical experiments, as the top gate electrode interferes with the optical path. A sufficiently transparent conducting material is therefore needed for the top electrode. Remarkably, the transparency requirement for near-field experiments is even more stringent than for far-field measurements, in particular close to the resonances of the structure, as discussed later.

The traditional choice as a top-gate material for 2D material samples is an evaporated gold film. In order to be transparent in the relevant optical range, the electrode thickness must be well below the skin depth of the material to avoid screening of the near-field electromagnetic field. Typical metals have a skin depth of tens of nanometres for infrared frequencies²⁰, which requires the metal film to be only few nanometres thick. Even in this case, as shown in the following, metallic thin films are not able to meet the more stringent requirements imposed by near-field experiments. On the other hand, conducting oxides, like Indium-Tin Oxide (ITO), are commonly used as transparent electrodes for visible light but are not transparent at infrared frequencies²¹.

Recent experiments²²⁻²⁴ have made advances in realizing a transparent top gate for s-SNOM experiments with 2D materials, which also provide atomically flat interfaces and allow for easier device integration. Single-layer graphene is sufficiently transparent to probe near-field signals through it²², yet its own plasmonic resonance interferes with the optical response of the material underneath, complicating the interpretation of the observed near-field signal^{23,24}. Still, for studying structural changes that do not involve collective resonances this is not an obstacle²². As alternative to graphene, the TMD MoS_2 has been used, which indeed does not host any resonances that disturb the near-field signal²³. However, since this material is unipolar due to Fermi level pinning at the contacts, it can only introduce p-type doping

Equation 1 shows that the reflection coefficient is not affected by the addition of the new layer ($r' \approx r$) when each

in the material below²⁵.

In this work, we show that WSe_2 can act as an infrared-transparent bipolar gate electrode for near-field experiments as schematically illustrated in Fig. 1. We validate its performance by studying the change in induced plasmon wavelength λ_p in bilayer graphene. This allows us to determine the carrier density induced by the top gate, while at the same time we characterize to what extent a charged top layer obstructs the observation of plasmons.

We first rigorously derive the transparency requirement for a top-gate electrode to be used in near-field optical experiments. The near field response of a homogeneous layered structure is completely determined by its reflection coefficient r for transverse magnetic (TM) waves (the coupling to transverse-electric modes is negligible in near-field) that is a function of the angular frequency ω and the in-plane wavevector q . Adding another thin layer (either a 2D material or a thin film of a bulk material) on top of the structure alters the reflection coefficient according to (see derivation in Sect. 2 of SI)

$$r' = r \frac{1 - S - r^{-1}S}{1 + S + rS}, \quad (1)$$

where r' is the reflection coefficient (function of ω and q) of the structure after the addition of the new layer and S quantifies the optical disturbance introduced by the new layer (as defined in Sect.2 of the SI). S depends on the optical conductivity of the new layer as

$$S(q, \omega) = \frac{\sigma_{2D}(q, \omega) \sqrt{\omega^2/c^2 - q^2}}{2\epsilon_0\omega}, \quad (2)$$

where σ_{2D} is the 2D longitudinal (in the direction of the wavevector) conductivity of the material, c is the speed of light, and ϵ_0 the vacuum permittivity. For 2D materials, σ_{2D} is directly the optical conductivity of the material (in Ω^{-1}), while for thin layers of three-dimensional conducting materials $\sigma_{2D} = \sigma\delta$, where σ is the optical conductivity and δ is the thickness of the layer (see detailed discussion in Sect.2 of the SI). We do not consider thick films since their impact on the optical signal is always stronger than that of thin films made of the same material.

of the three conditions $|S| \ll 1$, $|r|, |r|^{-1}$ is satisfied (note that $S = -1$ is the resonance condition of the new layer

when isolated, our conditions therefore imply the absence of resonances of the new layer). The reflection coefficient can be larger than one in absolute value when decaying fields are concerned (i.e. when $q > \omega/c$) and peak exactly at the positions of the collective oscillations²⁹, reaching values of the order of the quality factor Q of the collective oscillation. To observe a collective oscillation without distortion we therefore need $|S| \ll 1/Q$.

Figure 2 shows a comparison of the values of $|S|$ calculated, in the ranges of wavevector and frequency that are relevant in typical s-SNOM experiments, for single-layer graphene, trilayer WSe₂, and a 1 nm gold film. Most plasmonic excitations probed in room-temperature s-SNOM experiments have $Q \approx 10$. It is therefore not possible to study plasmonic excitations using graphene or gold films as a transparent top gate in the mid-infrared regime. In contrast, trilayer WSe₂ is well suited for this purpose, at least for photon energies above 100 meV.

The optical disturbance can be reduced by reducing the optical conductivity of the top-gate material, as shown in Eq. 2. For a material with a Drude-like response this can be done by reducing the carrier density and the relaxation

Figure 1 shows a schematic of the dual-gated device used in this experiment using WSe₂ as top gate. Our device consists of bilayer graphene (BLG) encapsulated in hexagonal boron nitride (hBN) with a thin WSe₂ staircase flake acting as a top gate, fabricated as described in the Methods (Sect. 1 of Supporting Information presents an optical image of our device). Given the rapid decay of the near-field signal in the out-of-plane direction, we use a 4 nm thin top hBN flake. The Si/SiO₂ bottom gate serves as a backgate to bring BLG into a highly doped state where plasmons do not suffer from Landau damping⁹. In addition, the bottom gate provides a reference for determining the plasmon wavelength λ_p as function of the induced carrier density n . Over the course of two months, we did not observe any signs of degradation of the WSe₂, despite performing the experiments in ambient conditions³⁵.

Figure 3a shows a near-field image of BLG with doping $n \sim 10^{13} \text{ cm}^{-2}$ induced by the bottom gate at $V_B = 80 \text{ V}$ along with photodoping, but with $V_T = 0$. Photodoping involves photoexciting defect states at the SiO₂/hBN interface^{8,36}, which effectively sets the charge-neutrality point V_D at -65 V , as extracted from the maximum of the measured source-drain resistance. The fringes running parallel to the BLG edge are a manifestation of plasmon polaritons, which we observe as both tip-launched edge-reflected ($\lambda_p/2$ period) and edge-launched (λ_p period)⁹, as explained in Methods.

To understand the peculiar shape of $\lambda_p(V_T)$ from a perspective of the electrostatics in our device, we first need to determine the induced carrier density in BLG by the WSe₂ top gate. To do so, we calibrate $\lambda_p(n)$ by using the bottom gate as a reference. According to Eq. (3) introduced below, when $V_T = 0 \text{ V}$ the induced carrier density can be described by a simple parallel plate capacitor only dependent on V_B . We measure the plasmon fringes along the same line cut while varying voltage on the bottom gate and keeping $V_T = 0 \text{ V}$ (Fig. 4c,d). Applying the same fitting procedure at each voltage point, we find a linear dependence of the plasmon wavelength on V_B , as is expected for

time or by increasing the effective mass. The carrier density is changing when the gate voltage is applied and for effective gating it cannot be smaller than $\approx 10^{12} \text{ cm}^{-2}$. Additionally, the scattering time τ is typically too long to play a role for mid-infrared frequencies. The search for better materials for top-gating should therefore be oriented towards materials with larger effective masses.

WSe₂ can be exfoliated down to a single layer^{30,31} of 0.7 nm and has relatively low mobilities up to $500 \text{ cm}^2/(\text{Vs})$ ^{27,30}. In contrast to MoS₂, WSe₂ is ambipolar and thus allows for injecting both carrier types³². A common issue arising with TMDs is the Schottky barrier forming at the metal-semiconductor interface, typically severely blocking transport through either the valence or conduction band. This can be overcome by a suitable choice of two different metals for the source and drain contact³³. However, since we intend to use WSe₂ solely as a gate electrode, a highly resistive contact does not pose an issue, provided we do not modulate the carrier density at high frequencies (Based on an estimated device resistance³⁴ of $\approx 40 \text{ k}\Omega$ and a geometrical capacitance of $\approx 0.8 \text{ pF}$ we obtain an RC cut-off frequency of $\approx 200 \text{ MHz}$).

As a next step, we apply a voltage V_T on the WSe₂ top gate while keeping BLG in the same highly doped state, and record the near-field signal along the arrow in Fig. 3a. At this location the top gate consists of three layers of WSe₂ with total thickness of $\approx 2.2 \text{ nm}$. Figure 3b demonstrates that by applying a voltage to the top gate we are able to change the observed plasmon wavelength. By fitting the oscillations to the model introduced in the Methods section, we determine the change in plasmon wavelength to be $\pm 10 \text{ nm}$ for $V_T = \pm 0.75 \text{ V}$. This means that WSe₂ is able to induce carriers of both types in BLG, and thus acts as an ambipolar top gate. In addition, the signal-to-noise ratio of near-field signal stays qualitatively constant while changing the top-gate voltage, confirming that the presence of the top gate does not affect the optical signal.

To study the response of the transparent top gate in more detail, we measure the near-field signal while systematically scanning the voltage on the top gate, shown in Fig. 4a. Judging by the fringe spacing for different V_T , these data suggest that the top gate only becomes ‘active’ for high $|V_T|$. To examine this quantitatively, we fit the data to Eq. (4) for each voltage, and extract the plasmon wavelength as function of top gate voltage (Fig. 4b). We find indeed a piece-wise linear function with an inactive region for low $|V_T|$, while the slope of $\lambda_p(V_T)$ is rather similar for $|V_T| > 0.4 \text{ V}$.

a two-dimensional conductor with parabolic bands³⁷. Using the capacitance of the bottom gate as mentioned below and $V_D = -74 \text{ V}$ in this measurement, we can convert voltages to carrier densities and fit the plasmon wavelength (Fig. 4d.) to a linear relation $\lambda_p = an + b$, yielding $a = 8.23 \cdot 10^{-12} \text{ nm} \cdot \text{cm}^2$ and $b = 34.5 \text{ nm}$. From this calibration, we can convert the measured change in plasmon wavelength (Fig. 4b) to the carrier density Δn induced by the WSe₂ top gate. The final result of our experiment is shown Figure 5a that displays the carrier density induced by the gate as a function of the top-gate voltage. Note that these measurements were obtained in a completely

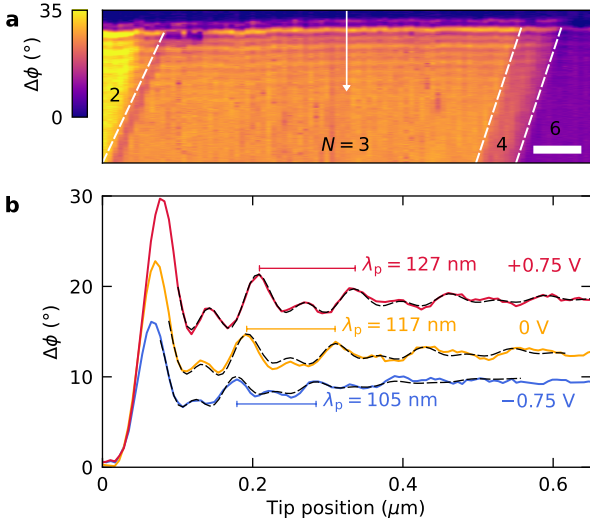


Fig. 3 | Controlling the plasmon wavelength with a WSe₂ top gate. **a** Spatial map of the near-field phase contrast at the edge of the bilayer graphene, corresponding to the yellow box in Fig. S1 in Supporting Information. The Silicon bottom gate induces a high carrier density $\sim 10^{13} \text{ cm}^{-2}$ ($V_B - V_D = 145 \text{ V}$), allowing the propagation of plasmon polaritons, as seen by the fringes running parallel to the edge. The area shown is covered by WSe₂ of various thicknesses, as indicated by the number of layers N . The excitation energy is 117 meV and the scale bar is 300 nm. **b** Line cuts along the white arrow in Fig. 3a demonstrate the effect of the WSe₂ top gate while keeping $V_B - V_D = 145 \text{ V}$. Without obstructing near-field access, applying a voltage to WSe₂ alters the carrier density in BLG (V_T indicated for each line cut), which affects the measured plasmon wavelength λ_p as extracted from a fit (black dashed lines).

optical way without relying on transport measurements on graphene. This demonstrates that graphene plasmons can act as independent local probes of the carrier density that can complement traditional transport measurements.

We can understand our results in terms of a simple model that relates the carrier density n in BLG for given gate voltages V_B and V_T . This is based on the equilibrium of the electrochemical potentials (see derivation in Sect. 4 of the Supporting Information) and leads to the relation

$$n = \frac{C_B(V_B - V_D)}{e} + \frac{C_T V_T}{e} + \frac{C_T \Delta\mu_{\text{WSe}_2}(V_T)}{e^2}, \quad (3)$$

where $C_T \approx 7.7 \text{ mF/m}^2$ and $C_B \approx 0.12 \text{ mF/m}^2$ are the geometric capacitances corresponding to the top and bottom gate, e is the unit charge, $\Delta\mu_{\text{WSe}_2}$ is the shift in chemical potential of WSe₂ with respect to its value at $V_T = 0 \text{ V}$, and the quantum capacitance of BLG $C_Q \approx 62 \text{ mF/m}^2$ has been ignored since it is much larger than $C_{T/B}$. From this equation we see that for $V_T = 0 \text{ V}$, the carrier density in BLG can be described by the geometric capacitance of the bottom gate (first term), which we used for the calibration of $\lambda_p(n)$ above. On the other hand, once we fix V_B , the change in carrier density is determined by the geometric capacitance of the top gate (second term) and the quantum capacitance of WSe₂ (last term). The interplay of the last two terms causes the step-like behaviour seen in Fig. 5a,

with the central flat region corresponding to the values of V_T for which the chemical potential falls deep in the gap of the semiconductor. The calculation of $\Delta\mu_{\text{WSe}_2}(V_T)$ is presented in Sect. 4 of the Supporting Information.

A band alignment diagram of WSe₂ and BLG explains the gating response in more detail (Fig. 5b). Starting with a BLG at a high carrier density induced by the bottom gate, the chemical potentials of WSe₂ and BLG are aligned for $V_T = 0 \text{ V}$. In this situation the chemical potential of WSe₂ resides within the energy gap of WSe₂. Upon increasing V_T , owing to the low quantum capacitance of WSe₂ in its insulating state, $\Delta\mu_{\text{WSe}_2}$ shifts down by V_T until it reaches the valence band. Once that happens, holes are introduced in the valence band and the capacitively induced electrons in BLG shift the chemical potential of BLG upwards. Due to the relatively high density of states of the valence band of WSe₂, its chemical potential remains close to the valence band edge for higher carrier densities. Since the difference in chemical potential between WSe₂ and BLG has to be equal to V_T , the bands of WSe₂ and BLG separate in energy for higher carrier densities.

In fitting the data to our model in Fig. 5a, we only leave the valence and conduction band energies as free fit parameters, while the other parameters can be estimated with sufficient accuracy. The fit yields a band gap of $(1.05 \pm 0.02) \text{ eV}$ (the error being estimated from the fitting procedure), and is almost perfectly centred at $V_T = 0 \text{ V}$. We theoretically calculated the electronic band gap and the densities of states at the band extrema of our material by performing Density Functional Theory (DFT) calculations for trilayer WSe₂ using the Atomic Simulations Recipe environment and the GPAW package^{38,39}. The electronic band structure and the densities of the states are reported in the S.I. We find an electronic band gap of 1.05 eV which agrees very well with the experimental results in this work and previous theoretical calculations^{26,40,41}. The agreement with the experiment is surprising because DFT is known to underestimate the band gaps, and generally the experimental band gap of trilayer WSe₂ is reported^{26,42,43} at higher values around 1.45 eV. We believe that this discrepancy is caused by the charge imbalance present in WSe₂ when generating an external electric field. The internal field due to the charge imbalance can modify the electronic bands and is expected to reduce the gap size due to band bending.

In summary, we have shown that few-layer WSe₂ can be used as a transparent ambipolar top gate for near-field experiments. This is demonstrated by tuning the plasmonic excitations in bilayer graphene via a WSe₂ top gate without obscuring the near-field scattering signal. Nanoscale measurements of the plasmon wavelength allow us to extract the gating efficiency, which we capture in a minimal model that considers the geometric and quantum capacitances. We expect other members of the TMD class, in particular those with higher effective masses, to be equally suitable as infrared transparent top gates due to their similarity, while their scalability via CVD growth allows for easy device integration^{44–47}. This work paves the way for future cryogenic near-field experiments on exotic states in dual-gated sample geometries^{15–19}. On the other hand, our experiment allowed to directly probe the energy gap and band-alignment (relative to graphene) of semiconducting 2D materials, pro-

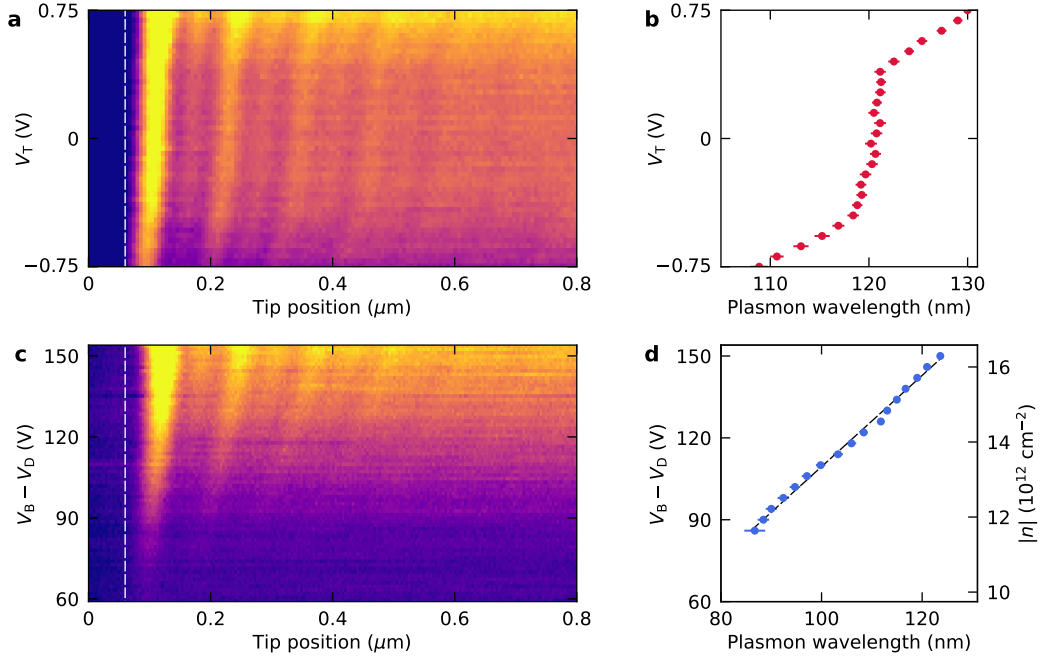


Fig. 4 | Systematically measuring the response of the WSe₂ top gate. **a** Line cut of the near-field phase signal along the white arrow in Fig. 3a for a range of top gate voltages, while $V_B - V_D = 145$ V. The edge of bilayer graphene is marked with a dashed line. Colour scale is the same as in Fig. 3a, covering 18 degree phase difference. **b** The extracted plasmon wavelength shows a piece-wise linear dependence on the top gate voltage. The error bars represent $\pm 1\sigma$. **c** Near-field phase signal along the same line as panel **a** for a range of bottom gate voltages ($V_T = 0$ V), serving as calibration to determine the carrier density induced by the WSe₂ top gate. **d** The extracted plasmon wavelength scales approximately linear with the bottom gate voltage and carrier density, as indicated by a linear fit (dashed line).

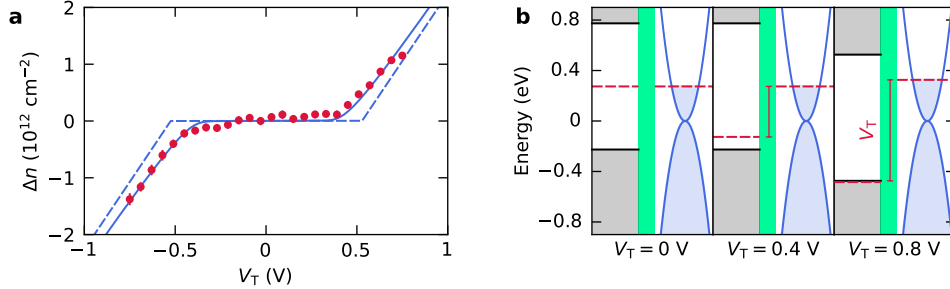


Fig. 5 | Gating efficiency of trilayer WSe₂ and band alignment. **a** Induced shift in the carrier density Δn in BLG by applying a voltage to WSe₂ through a 4 nm hBN layer. The flat response for small top gate voltages ($|V_T| < 0.4$ V) arises from the intrinsic gap in WSe₂, while for larger voltages ($|V_T| > 0.4$ V) WSe₂ acts as a conductor and the slope is determined by the geometric capacitance. From a fit according to the electrostatic model with $T = 300$ K we extract a gap of 1.05 eV in WSe₂ (solid line). The dashed line represents the calculated Δn at zero temperature using the same fit parameters. **b** Band alignment of semiconducting WSe₂ (grey bands) with respect to BLG (blue bands) for three different positive top gate voltages. For small V_T , the chemical potential of WSe₂ shifts down by V_T (middle panel). Once V_T is large enough that the chemical potential of WSe₂ reaches the valence band edge, carriers are injected into BLG moving its chemical potential upwards (right panel). At the same time, the bands of WSe₂ and BLG are shifted apart such that the V_T equals the difference in chemical potentials, indicated by the vertical bar.

viding information that can complement the data obtained by other techniques⁴⁸.

METHODS

Device fabrication

To fabricate the hBN (25 nm)/BLG/hBN (4 nm)/WSe₂ heterostructure depicted in Fig. 1, we used a standard stacking method⁴⁹. First, we exfoliate from WSe₂ crystals (HQ Graphene) a thin staircase flake that acts as a top gate. Making use of a stamp of polydimethylsiloxane (PDMS)

covered by a thin polycarbonate film, we pick up the WSe₂ flake, followed by the hBN and BLG flakes. These steps are performed at 40 °C, while the final stack is deposited on the Si/SiO₂ target substrate at 165 °C to assist in squeezing out any bubbles⁵⁰. Low-resistance contacts to BLG are made by reactive ion etching in a CHF₃/O₂ gas mixture, followed by Cr/Au metallization⁵¹. The WSe₂ flake is contacted with Ti/Au with the aim to avoid a high Schottky barrier. However, we found in other devices that Cr/Au provides an equally well-functioning contact to a WSe₂ top gate. Finally, to prepare the device for s-SNOM measurements, we mechanically cleaned the top surface using contact-mode Atomic Force Microscope (AFM) brooming⁵².

Measurement details

The near-field measurements have been performed on the neaSNOM platform (neaspec), equipped with a CO₂ gas laser (Access Laser) and a fast HgCdTe detector (Kolmar Technologies). We focus 15 mW of infrared light (wavelength 10.6 μm, corresponding to a photon energy of 117 meV) onto a PtIr-coated AFM tip (Nanoworld), which oscillates at a frequency ≈ 250 kHz with a tapping amplitude of 80 – 100 nm. We operate the system in a pseudoheterodyne mode⁵³ using a ZnSe beam splitter to obtain the phase resolved near-field signal. To avoid detecting unwanted far-field signals, we record the near-field signal at the third harmonic of the cantilever oscillation. All measurements are performed in ambient conditions.

Extraction of plasmon wavelength

The hotspot at the tip interacts with the charge carriers in graphene and produces collective excitations that are reflected by interfaces, return to the tip, and are finally converted into a scattered field, as measured by the infrared photodetector. This leads to oscillations in the near-field signal, as seen in Figure 3. Because plasmons make a round trip, peaks in the near-field signal occur at half the plasmon wavelength, satisfying constructive interference underneath the tip. In addition to these tip-launched plasmons, the graphene edge can also act as a launcher. In that case, the near-field signal underneath the tip is modulated at a spacing equal to the plasmon wavelength. We determine the plasmon wavelength $\lambda_p = 2\pi/q_1$ using the model introduced in Ref. 9, which accounts for both contributions in the optical signal:

$$s_{\text{opt}}(x) = A \frac{e^{i2qx}}{\sqrt{x}} + B \frac{e^{iqx}}{x^\alpha} + Cx + D, \quad (4)$$

with x as the distance from the graphene edge to the tip position, and $q = q_1 + iq_2$ as the complex plasmon wavevector. The first term describes tip-launched plasmons that decay on a scale $\propto 1/q_2$, and takes into account a geometrical decay factor \sqrt{x} . The second term accounts for edge-launched plasmons with a variable decay factor $\alpha \sim 1$. A , B are complex fit parameters, and $Cx + D$ captures any offsets in the signal.

REFERENCES

- [1] Novotny, L. & Stranick, S. J. Near-field optical microscopy and spectroscopy with pointed probes. *Annu. Rev. Phys. Chem.* **57**, 303–331 (2006).
- [2] Chen, J. et al. Optical nano-imaging of gate-tunable graphene plasmons. *Nature* **487**, 77–81 (2012).
- [3] Fei, Z. et al. Gate-tuning of graphene plasmons revealed by infrared nano-imaging. *Nature* **487**, 82–85 (2012).
- [4] Dai, S. et al. Tunable Phonon Polaritons in Atomically Thin van der Waals Crystals of Boron Nitride. *Science* **343**, 1125–1129 (2014).
- [5] Basov, D. N., Asenjo-Garcia, A., Schuck, P. J., Zhu, X. & Rubio, A. Polariton panorama. *Nanophotonics* **10**, 549–577 (2021).
- [6] Basov, D. N., Fogler, M. M. & Garcia de Abajo, F. J. Polaritons in van der Waals materials. *Science* **354** (2016).
- [7] Low, T. et al. Polaritons in layered two-dimensional materials. *Nature Materials* **16**, 182–194 (2017).
- [8] Woessner, A. et al. Near-field photocurrent nanoscopy on bare and encapsulated graphene. *Nature Communications* **7**, 10783 (2016).
- [9] Woessner, A. et al. Highly confined low-loss plasmons in graphene–boron nitride heterostructures. *Nature Materials* **14**, 421–425 (2015).
- [10] Ni, G. X. et al. Fundamental limits to graphene plasmonics. *Nature* **557**, 530–533 (2018).
- [11] Lundeberg, M. B. et al. Tuning quantum nonlocal effects in graphene plasmonics. *Science* **357**, 187–191 (2017).
- [12] Sunku, S. S. et al. Photonic crystals for nano-light in moiré graphene superlattices. *Science* **362**, 1153–1156 (2018).
- [13] Schmidt, P. et al. Nano-imaging of intersubband transitions in van der Waals quantum wells. *Nature Nanotechnology* **13**, 1035–1041 (2018).
- [14] McCann, E. & Koshino, M. The electronic properties of bilayer graphene. *Reports on Progress in Physics* **76**, 056503 (2013).
- [15] Hasdeo, E. H. & Song, J. C. W. Long-Lived Domain Wall Plasmons in Gapped Bilayer Graphene. *Nano Letters* **17**, 7252–7257 (2017).
- [16] Liu, X. et al. Tunable spin-polarized correlated states in twisted double bilayer graphene. *Nature* **583**, 221–225 (2020).
- [17] Cao, Y. et al. Tunable correlated states and spin-polarized phases in twisted bilayer–bilayer graphene. *Nature* **583**, 215–220 (2020).
- [18] Park, J. M., Cao, Y., Watanabe, K., Taniguchi, T. & Jarillo-Herrero, P. Tunable strongly coupled superconductivity in magic-angle twisted trilayer graphene. *Nature* **590**, 249–255 (2021).
- [19] Hao, Z. et al. Electric field-tunable superconductivity in alternating-twist magic-angle trilayer graphene. *Science* **371**, 1133–1138 (2021).
- [20] Rahman, F. *Nanostructures in Electronics and Photonics* (Pan Stanford, 2016).
- [21] Amalric-Popescu, D. & Bozon-Verduraz, F. Infrared studies on sno2 and pd/sno2. *Catalysis Today* **70**, 139–154 (2001). A tribute to Jean-Claude Lavalley.
- [22] Li, H. et al. Global Control of Stacking-Order Phase Transition by Doping and Electric Field in Few-Layer Graphene. *Nano Letters* **20**, 3106–3112 (2020).
- [23] Sunku, S. S. et al. Dual-Gated Graphene Devices for Near-Field Nano-imaging. *Nano Letters* **21**, 1688–1693 (2021).
- [24] Luo, W. et al. Nanoinfrared Characterization of Bilayer Graphene Conductivity under Dual-Gate Tuning. *Nano Letters* **21**, 5151–5157 (2021).

- [25] Kim, C. et al. **Fermi Level Pinning at Electrical Metal Contacts of Monolayer Molybdenum Dichalcogenides**. *ACS Nano* **11**, 1588–1596 (2017).
- [26] Movva, H. C. et al. **Tunable Γ -K Valley Populations in Hole-Doped Trilayer WSe_2** . *Physical Review Letters* **120**, 107703 (2018).
- [27] Movva, H. C. P. et al. **High-Mobility Holes in Dual-Gated WSe_2 Field-Effect Transistors**. *ACS Nano* **9**, 10402–10410 (2015).
- [28] Johnson, P. B. & Christy, R. W. **Optical constants of the noble metals**. *Phys. Rev. B* **6**, 4370–4379 (1972).
- [29] Gonçalves, P. A. D. & Peres, N. M. R. **An introduction to graphene plasmonics** (World Scientific, Singapore, 2016).
- [30] Podzorov, V., Gershenson, M. E., Kloc, C., Zeis, R. & Bucher, E. **High-mobility field-effect transistors based on transition metal dichalcogenides**. *Applied Physics Letters* **84**, 3301–3303 (2004).
- [31] Fang, H. et al. **High-Performance Single Layered WSe_2 p-FETs with Chemically Doped Contacts**. *Nano Letters* **12**, 3788–3792 (2012).
- [32] Wang, Z. et al. **The ambipolar transport behavior of WSe_2 transistors and its analogue circuits**. *NPG Asia Materials* **10**, 703–712 (2018).
- [33] Das, S. & Appenzeller, J. **WSe_2 field effect transistors with enhanced ambipolar characteristics**. *Applied Physics Letters* **103**, 103501 (2013).
- [34] Chuang, H.-J. et al. **Low-resistance 2d/2d ohmic contacts: A universal approach to high-performance wse_2 , mos_2 , and $mose_2$ transistors**. *Nano Letters* **16**, 1896–1902 (2016). PMID: 26844954.
- [35] Gammelgaard, L., Whelan, P. R., Booth, T. J. & Bøggild, P. **Long-term stability and tree-ring oxidation of wse_2 using phase-contrast afm**. *Nanoscale* **13**, 19238–19246 (2021).
- [36] Ju, L. et al. **Photoinduced doping in heterostructures of graphene and boron nitride**. *Nature Nanotechnology* **9**, 348–352 (2014).
- [37] Low, T., Guinea, F., Yan, H., Xia, F. & Avouris, P. **Novel Midinfrared Plasmonic Properties of Bilayer Graphene**. *Physical Review Letters* **112**, 116801 (2014).
- [38] Gjerding, M. et al. **Atomic simulation recipes: A python framework and library for automated workflows**. *Computational Materials Science* **199**, 110731 (2021).
- [39] Enkovaara, J. et al. **Electronic structure calculations with gpaw: a real-space implementation of the projector augmented-wave method**. *Journal of physics: Condensed matter* **22**, 253202 (2010).
- [40] Dai, X., Li, W., Wang, T., Wang, X. & Zhai, C. **Bandstructure modulation of two-dimensional WSe_2 by electric field**. *Journal of Applied Physics* **117** (2015).
- [41] Javaid, M., Russo, S. P., Kalantar-Zadeh, K., Greentree, A. D. & Drumm, D. W. **Band structure and giant Stark effect in two-dimensional transition-metal dichalcogenides**. *Electronic Structure* **1**, 015005 (2018).
- [42] Zhao, W. et al. **Evolution of Electronic Structure in Atomically Thin Sheets of WS_2 and WSe_2** . *ACS Nano* **7**, 791–797 (2013).
- [43] Zeng, H. et al. **Optical signature of symmetry variations and spin-valley coupling in atomically thin tungsten dichalcogenides**. *Scientific Reports* **3**, 1608 (2013).
- [44] Lin, Y.-C. et al. **Direct Synthesis of van der Waals Solids**. *ACS Nano* **8**, 3715–3723 (2014).
- [45] Wang, X. et al. **Chemical Vapor Deposition Growth of Crystalline Monolayer $MoSe_2$** . *ACS Nano* **8**, 5125–5131 (2014).
- [46] Eichfeld, S. M. et al. **Highly Scalable, Atomically Thin WSe_2 Grown via Metal–Organic Chemical Vapor Deposition**. *ACS Nano* **9**, 2080–2087 (2015).
- [47] Liu, B. et al. **Chemical Vapor Deposition Growth of Monolayer WSe_2 with Tunable Device Characteristics and Growth Mechanism Study**. *ACS Nano* **9**, 6119–6127 (2015).
- [48] Gutiérrez-Lezama, I., Ubrig, N., Ponomarev, E. & Morpurgo, A. F. **Ionic gate spectroscopy of 2d semiconductors**. *Nature Reviews Physics* **3**, 508 (2021).
- [49] Zomer, P. J., Guimarães, M. H. D., Brant, J. C., Tombros, N. & van Wees, B. J. **Fast pick up technique for high quality heterostructures of bilayer graphene and hexagonal boron nitride**. *Applied Physics Letters* **105**, 013101 (2014).
- [50] Purdie, D. G. et al. **Cleaning interfaces in layered materials heterostructures**. *Nature Communications* **9**, 5387 (2018).
- [51] Wang, L. et al. **One-Dimensional Electrical Contact to a Two-Dimensional Material**. *Science* **342**, 614–617 (2013).
- [52] Goossens, A. M. et al. **Mechanical cleaning of graphene**. *Applied Physics Letters* **100**, 073110 (2012).
- [53] Ocelic, N., Huber, A. & Hillenbrand, R. **Pseudoheterodyne detection for background-free near-field spectroscopy**. *Applied Physics Letters* **89**, 101124 (2006).

ACKNOWLEDGEMENTS

F.H.L.K. acknowledges financial support from the Government of Catalonia through the SGR grant, and from the Spanish Ministry of Economy and Competitiveness, through the Severo Ochoa Programme for Centres of Excellence in R&D (Ref. SEV-2015-0522), and Explora Ciencia (Ref. FIS2017-91599-EXP). F.H.L.K. also acknowledges support by Fundacio Cellex Barcelona, Generalitat de Catalunya through the CERCA program, and the Mineco grant Plan Nacional (Ref. FIS2016-81044-P) and the Agency for Management of University and Research Grants (AGAUR) (Ref. 2017-SGR-1656). Furthermore, the research leading to these results has received funding from the European Union's Horizon 2020 programme under grant agreements Refs. 785219 (Graphene Flagship Core2) and 881603 (Graphene Flagship Core3), and Ref. 820378 (Quantum Flagship). This work was supported by the ERC TOPONANOP under grant agreement Ref. 726001. N.C.H.H. acknowledges funding from the European Union's Horizon 2020 research and innovation programme under the Marie Skłodowska-Curie grant agreement Ref. 665884. I.T. acknowledges funding from the Spanish Ministry of Science, Innovation and Universities (MCIU) and State Research Agency (AEI) via the Juan de la Cierva fellowship Ref. FJC2018-037098-I. K.W. and T.T. acknowledge support from JSPS KAKENHI (Grant Numbers 19H05790, 20H00354 and 21H05233). K.S.T. acknowledge funding from the European Research Council (ERC) Grant No. 773122 (LIMA). K.S.T. is a Villum Investigator supported by VILLUM FONDEN (grant no. 37789).

AUTHOR CONTRIBUTIONS

N.C.H.H. and F.H.L.K. conceived the experiment. N.C.H.H. fabricated the devices and performed the experiments. K.W. and T.T. synthesized the hBN crystals. I.T. developed the theoretical modeling of the experiment. M.K.S. and K.S.T. performed the DFT band-structure calculations. N.C.H.H., I.T. and F.H.L.K. analysed the results

and wrote the manuscript with input from all the authors.
F.H.L.K. supervised the work.

COMPETING FINANCIAL INTERESTS

The authors declare no competing financial interests.

DATA AVAILABILITY STATEMENT

The data that support the plots within this paper and other findings of this study are available from the corresponding author upon reasonable request.

Supporting information for "WSe₂ as transparent top gate for near-field experiments"

I. DEVICE GEOMETRY

Figure S1 shows an optical image of the device featured in the main text. The stack was etched in the dark purple regions, providing a reflecting interface for plasmons. The yellow rectangle corresponds to the scan of Fig. 3a in the main text.

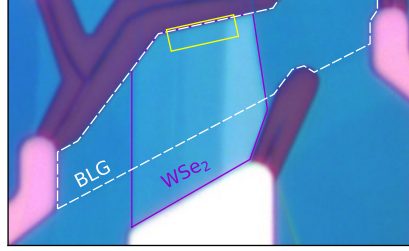


Fig. S1 | Optical image of our device. The locations of bilayer graphene and WSe₂ flakes are indicated by a dashed white line and a solid purple line respectively.

II. REFLECTION PERTURBATION INDUCED BY AN ADDITIONAL LAYER

We consider the transmission of electromagnetic fields inside homogeneous layered structures made of uniaxial dielectrics with the special axis oriented in the stacking direction \hat{z} . The description of electromagnetic fields can be separated in Transverse Electric (TE) and Transverse Magnetic (TM) modes, with only the latter having a significant coupling to near-field probes. Defining the direction of in-plane propagation as \hat{x} , TM fields in homogeneous planar structures can be conveniently described in terms of the vector

$$\mathbf{v}(z) = \begin{pmatrix} E_x(z) \\ Z_0 H_y(z) \end{pmatrix}, \quad (\text{S1})$$

where \mathbf{E} is the electric field, \mathbf{H} is the magnetic field, $Z_0 = \sqrt{\mu_0/\epsilon_0} \approx 377 \Omega$ is the vacuum impedance, and all the fields have the form $\mathbf{F}(\mathbf{r}, t) = \mathbf{F}(z)e^{iqx - i\omega t}$. With this notation Maxwell's equations reduce, in a uniform layer and for the relevant polarization, to the first-order differential equation

$$\frac{d}{dz}\mathbf{v}(z) = iK\mathbf{v}(z), \quad (\text{S2})$$

where

$$K = \begin{pmatrix} 0 & \frac{cq_z^2}{\omega\epsilon_{\parallel}} \\ \frac{\omega}{c}\epsilon_{\parallel} & 0 \end{pmatrix} \quad (\text{S3})$$

and

$$q_z = \xi \sqrt{\frac{\omega^2}{c^2}\epsilon_{\parallel}\mu_{\parallel} - \frac{\epsilon_{\parallel}}{\epsilon_{\perp}}q^2}. \quad (\text{S4})$$

Here the optical constant of the material are in the form $\epsilon = \text{diag}(\epsilon_{\parallel}, \epsilon_{\parallel}, \epsilon_{\perp})$, and $\mu = \text{diag}(\mu_{\parallel}, \mu_{\parallel}, \mu_{\perp})$, q is the in-plane wave vector, and the sign $\xi = \pm 1$ is chosen such that $\Im m[q_z] \geq 0$ and, in case $\Im m[q_z] = 0$, $\Re e[q_z] \geq 0$. The solution of (S2) in a uniform layer allows to relate the fields on the top of the layer to the ones at the bottom of the layer as

$$\mathbf{v}_{\text{top}} = M_{\text{layer}} \cdot \mathbf{v}_{\text{bottom}}, \quad (\text{S5})$$

where M_{layer} is the transfer matrix of the layer, which reads

$$M_{\text{layer}} = \exp[i\delta K] = \begin{pmatrix} \cos(q_z\delta) & i \sin(q_z\delta) \frac{cq_z}{\omega\epsilon_{\parallel}} \\ i \sin(q_z\delta) \frac{\omega\epsilon_{\parallel}}{cq_z} & \cos(q_z\delta) \end{pmatrix} \quad (\text{S6})$$

is the transfer matrix of the layer, with δ being the layer thickness.

A homogeneous layer supports two independent solutions corresponding to the two eigenvectors of K with corresponding eigenvalues $\pm q_z$, corresponding to the upwards (downwards) propagating wave. The general solution reads

$$\mathbf{v}(z) = A_+ e^{iq_z z} \begin{pmatrix} 1 \\ \frac{\omega \epsilon_{\parallel}}{cq_z} \end{pmatrix} + A_- e^{-iq_z z} \begin{pmatrix} 1 \\ -\frac{\omega \epsilon_{\parallel}}{cq_z} \end{pmatrix} \quad (\text{S7})$$

with A_{\pm} being the amplitudes of the two waves.

In a similar way the fields on the top and on the bottom of a two-dimensional conducting, non-magnetic sheet are connected by the boundary conditions on the electric and magnetic field. This relation can be expressed as

$$\mathbf{v}_{\text{top}} = M_{\text{sheet}} \cdot \mathbf{v}_{\text{bottom}}, \quad (\text{S8})$$

with M_{sheet} being the transfer matrix of a 2D sheet

$$M_{\text{sheet}} = \begin{pmatrix} 1 & 0 \\ -\sigma^{2D} Z_0 & 1 \end{pmatrix}. \quad (\text{S9})$$

The total transfer matrix of a structure composed of many layers and sheets is given by the matrix product of the individual layers $M_{\text{structure}} = M_N \cdot M_{N-1} \cdots M_1$.

The reflection r and transmission t coefficients (for the electric field) can be obtained by imposing scattering boundaries conditions. This means that above the structure the field is given by an incident wave propagating towards $-z$ and a reflected wave propagating towards $+z$, while underneath the structure there is only a transmitted wave propagating towards $-z$. Making use of (S7) and relating the field on the top and bottom of the structure via the total transfer matrix we obtain

$$\begin{pmatrix} 1 \\ -\frac{\omega \epsilon_{\parallel}^T}{cq_z^T} \end{pmatrix} + r \begin{pmatrix} 1 \\ \frac{\omega \epsilon_{\parallel}^T}{cq_z^T} \end{pmatrix} = t M_{\text{structure}} \cdot \begin{pmatrix} 1 \\ -\frac{\omega \epsilon_{\parallel}^B}{cq_z^B} \end{pmatrix} = t \begin{pmatrix} a \\ b \end{pmatrix}, \quad (\text{S10})$$

where the superscripts T and B denote the medium that is on the top and on the bottom of the structure.

In the same way after adding a new element to the structure characterized by a transfer matrix M' we can obtain the modified reflection and transmission coefficients r' and t' from

$$\begin{pmatrix} 1 \\ -\frac{\omega \epsilon_{\parallel}^T}{cq_z^T} \end{pmatrix} + r' \begin{pmatrix} 1 \\ \frac{\omega \epsilon_{\parallel}^T}{cq_z^T} \end{pmatrix} = t' M' \cdot M_{\text{structure}} \cdot \begin{pmatrix} 1 \\ -\frac{\omega \epsilon_{\parallel}^B}{cq_z^B} \end{pmatrix} = t' \begin{pmatrix} a' \\ b' \end{pmatrix}. \quad (\text{S11})$$

We can then relate r' to r by comparing (S10-S11) and using

$$\frac{a'}{b'} = \frac{M'_{11} \frac{a}{b} + M'_{12}}{M'_{22} + M'_{21} \frac{a}{b}}, \quad (\text{S12})$$

from which we obtain

$$\frac{r'}{r} = \frac{\frac{1}{2} \left(M'_{11} + M'_{22} + \frac{\omega \epsilon_{\parallel}^T}{cq_z^T} M'_{12} + \frac{cq_z^T}{\omega \epsilon_{\parallel}^T} M'_{21} \right) + r^{-1} \frac{1}{2} \left(M'_{11} - M'_{22} - \frac{\omega \epsilon_{\parallel}^T}{cq_z^T} M'_{12} + \frac{cq_z^T}{\omega \epsilon_{\parallel}^T} M'_{21} \right)}{\frac{1}{2} \left(M'_{11} + M'_{22} - \frac{\omega \epsilon_{\parallel}^T}{cq_z^T} M'_{12} - \frac{cq_z^T}{\omega \epsilon_{\parallel}^T} M'_{21} \right) + r \frac{1}{2} \left(M'_{11} - M'_{22} + \frac{\omega \epsilon_{\parallel}^T}{cq_z^T} M'_{12} - \frac{cq_z^T}{\omega \epsilon_{\parallel}^T} M'_{21} \right)}. \quad (\text{S13})$$

This equation holds in general and relates the reflection coefficient in the presence of the additional layer r' to the original reflection coefficient of the structure r . Specializing (S13) to a two-dimensional sheet with M' given by (S9) yields Eq. (1) of the main text

$$\frac{r'}{r} = \frac{1 - S - Sr^{-1}}{1 + S + rS}, \quad (\text{S14})$$

with

$$S = \frac{cZ_0 \sigma^{2D} q_z^T}{2\omega \epsilon_{\parallel}^T}, \quad (\text{S15})$$

that reduces to Eq. (2) of the main text if the material on top of the structure is vacuum.

For a 3D layer with a finite thickness δ the transfer matrix M' is given by (S6) and the general formula (S13) reduces to

$$\frac{r'}{r} = \frac{1 - S \left[1 + \left(\frac{q_z \epsilon_{\parallel}^T}{q_z^T \epsilon_{\parallel}} \right)^2 \right] - Sr^{-1} \left[1 - \left(\frac{q_z \epsilon_{\parallel}^T}{q_z^T \epsilon_{\parallel}} \right)^2 \right]}{1 + S \left[1 + \left(\frac{q_z \epsilon_{\parallel}^T}{q_z^T \epsilon_{\parallel}} \right)^2 \right] + rS \left[1 - \left(\frac{q_z \epsilon_{\parallel}^T}{q_z^T \epsilon_{\parallel}} \right)^2 \right]}, \quad (\text{S16})$$

with S given by

$$S = -\frac{i}{2} \tan(q_z \delta) \frac{q_z^T \epsilon_{\parallel}}{q_z \epsilon_{\parallel}^T}. \quad (\text{S17})$$

When near-field is concerned ($q \gg \omega/c$) and for an isotropic, non-magnetic material, with optical conductivity σ that is sufficiently large ($|\sigma| \gg \omega \epsilon_0$, as it is the case for metals below their plasma frequency) the quantities in square brackets in (S16) are close to one, recovering the same form of (S14). If moreover the thin-film condition $|q_z| \delta \ll 1$ is fulfilled (and again $|\sigma| \gg \omega \epsilon_0$) Eq. (S17) also reduces to Eq. (S15) with a 2D conductivity given by $\sigma^{2D} = \delta \sigma$.

III. ENERGY BAND STRUCTURE OF WSe₂

To calculate the electronic structure of the WSe₂ trilayer, we employ the Atomic Simulation Recipe (ASR) framework with GPAW as the electronic structure code.^{S1S2} To obtain the atomic structure, we start from the relaxed WSe₂ monolayer downloaded from the C2DB database^{S3.S4}, which we stack three copies of in the optimal 2H-stacking configuration. Subsequently, the structure is relaxed using the PBE-D3 scheme to account for van der Waals interactions.^{S5} We then perform a ground state calculation. The calculations were performed in plane-wave mode with a energy cut-off of 800 eV on a Γ -point centered K -point grid with a density of 12000 points/ \AA^2 . Spin-orbit coupling was included perturbatively. Based on the ground state calculation, we can obtain the electronic band structure, the effective masses of both electrons and holes, and the density of states, using the ASR bandstructure recipe, the ASR effective masses recipe, and the ASR pdos recipe respectively.

We find an electronic band gap of 1.05 eV. The effective mass of the valence band maximum is isotropic at 0.36 electron masses, m_e , and the effective mass of the conduction band is anisotropic with an effective mass of 0.46 m_e in the fast direction and 0.58 m_e in the slow direction. Based on the calculated density of states, we can estimate the effective density of states at the conduction band edge, N_c , and valence band edge, N_v ,

$$N_v = \int_{-\infty}^{E_v} dE \text{DOS}(E) \exp[(E - E_v)/(kT)] = 1.3 \cdot 10^{17} \text{ states} \cdot \text{m}^{-2}, \quad (\text{S18})$$

$$N_c = \int_{E_c}^{\infty} dE \text{DOS}(E) \exp[-(E - E_c)/(kT)] = 2.2 \cdot 10^{17} \text{ states} \cdot \text{m}^{-2}. \quad (\text{S19})$$

To model the gating efficiency of our WSe₂ gate we approximate the density of states with two constants $g_{v/c}$, below and above the gap respectively, chosen to reproduce the calculated effective densities of stats. These read

$$g_v = N_v/(kBT) = 4.9 \cdot 10^{18} \text{ states} \cdot \text{m}^{-2} \cdot \text{eV}^{-1}, \quad (\text{S20})$$

$$g_c = N_c/(kBT) = 8.5 \cdot 10^{18} \text{ states} \cdot \text{m}^{-2} \cdot \text{eV}^{-1}. \quad (\text{S21})$$

IV. CARRIER DENSITY IN GRAPHENE AS A FUNCTION OF THE TOP AND BOTTOM GATE VOLTAGES

Here we derive a minimal model, based on electrostatics and equilibrium of *electrochemical* potential, to calculate the density of carriers in graphene as a function of the top and bottom gate voltages. The main source of deviation from a purely electrostatic behavior is the quantum capacitance of the WSe₂ that becomes very small when the chemical potential is pushed deeply inside the gap due to the vanishing density of states, hence dominating over all the other capacities (that are summed in series).

In this simplified model we consider both bilayer graphene (BLG) and few-layer WSe₂ as perfectly two-dimensional materials neglecting the electrostatic potential drop between the different layers. To be consistent with this assumption we also neglect the modification of the BLG band structure due to the presence of an out-of-plane field and the corresponding gap-opening.

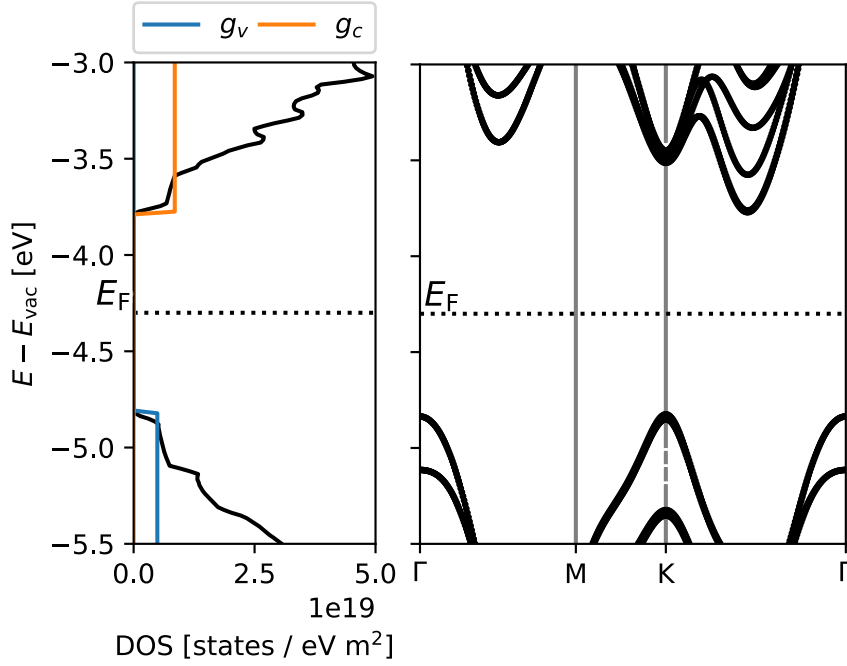


Fig. S2 | Left: density of states for a 2H-stacked trilayer of WSe₂. Blue and orange lines represent the approximate densities of states of the valence and conduction band respectively used in the actual modeling of the gating response. Right: DFT calculated electronic band structure for a 2H-stacked trilayer of WSe₂ in the relevant energy range along the $\Gamma MK\Gamma$ contour.

A. Electrostatics

We start by solving the Poisson equation in our structure. Neglecting edge effects this reads (in International System units)

$$-\partial_z[\epsilon_0\epsilon_\perp(z)\partial_z\phi(z)] = \rho(z), \quad (\text{S22})$$

where $\phi(z)$ is the electrostatic potential as a function of the out-of plane coordinate z , $\rho(z)$ is the density of charges not bound in dielectrics, $\epsilon_0 \approx 8.85 \cdot 10^{-12}$ F/m is the vacuum permittivity, and $\epsilon_\perp(z)$ is the relative dielectric permittivity of the structure. This is given by (See Fig. S3)

$$\epsilon_\perp(z) = \begin{cases} \epsilon_{\text{SiO}_2} \approx 4.1 & -t_1 - t_2 < z < -t_2 \\ \epsilon_{\text{hBN}\perp} \approx 3.5 & -t_2 < z < t_3. \end{cases} \quad (\text{S23})$$

Since no free charge is hosted in the dielectrics we can write the charge density as

$$\rho(z) = \rho_{\text{WSe}_2}\delta(z - t_3) + \rho_{\text{BLG}}\delta(z) + \rho_{\text{Si}}\delta(z + t_1 + t_2). \quad (\text{S24})$$

Note that in writing (S24) we have neglected the charge density that can build up at the hBN-SiO₂ interface due to photodoping. This contribution is difficult to quantify and only results in a rigid shift of the BLG carrier density. Since the device is overall neutral the three surface charge densities sum to zero

$$\rho_{\text{WSe}_2} + \rho_{\text{BLG}} + \rho_{\text{Si}} = 0. \quad (\text{S25})$$

Under the condition of vanishing electric field for $z > t_3$ and $z < -t_1 - t_2$, Eq. (S22) can be solved yielding a continuous, piecewise linear function

$$\phi(z) = \begin{cases} \phi_{\text{WSe}_2}\frac{z}{t_3} + \phi_{\text{BLG}}\frac{z-t_3}{-t_3} & 0 < z < t_3 \\ \phi_{\text{BLG}}\frac{z+t_2}{t_2} + \phi_1\frac{z}{-t_2} & -t_2 < z < 0 \\ \phi_1\frac{z+t_2+t_1}{t_1} + \phi_{\text{Si}}\frac{z+t_2}{-t_1} & -t_1 - t_2 < z < -t_2, \end{cases} \quad (\text{S26})$$

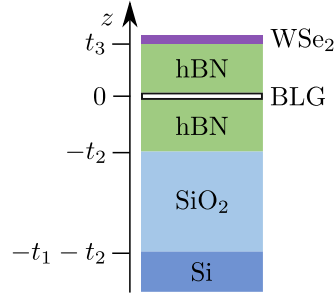


Fig. S3 | Scheme of the cross-section of our device. The origin of the z coordinate is taken at the position of the BLG layer. The thicknesses of the layers (out of scale) are $t_1 = 285$ nm, $t_2 = 25$ nm, and $t_3 = 4$ nm.

where the values of the electrostatic potential at the interfaces are given by

$$\phi_{\text{WSe}_2} = \frac{\rho_{\text{WSe}_2}}{C_T} \quad (\text{S27})$$

$$\phi_{\text{BLG}} = 0 \quad (\text{S28})$$

$$\phi_1 = \frac{\rho_{\text{Si}} t_2}{\epsilon_0 \epsilon_{\text{hBN}\perp}} \quad (\text{S29})$$

$$\phi_{\text{Si}} = \frac{\rho_{\text{Si}}}{C_B}. \quad (\text{S30})$$

Here, we specified the overall additive constant by requiring the electrostatic potential to vanish at the position of the BLG layer, while the two capacities are given by $C_T = \epsilon_0 \epsilon_{\text{hBN}\perp} / t_3 \approx 7.7$ mF/m² and $C_B = [(\epsilon_0 \epsilon_{\text{hBN}\perp} / t_2)^{-1} + (\epsilon_0 \epsilon_{\text{SiO}_2} / t_1)^{-1}]^{-1} \approx 0.12$ mF/m².

B. Quantum capacitances

The equilibrium conditions between the different layers are expressed in terms of the electrochemical potential Φ . This is defined for each layer as

$$-e\Phi_\alpha = -e\phi_\alpha + \mu_\alpha, \quad (\text{S31})$$

where $\alpha = \text{WSe}_2, \text{BLG}, \text{Si}$ and μ_α is the chemical potential measured from the vacuum level. We therefore need a relation between the charge density and the chemical potential in each layer.

In silicon, due to the large density of states we can neglect the shift in chemical potential due to the induced charge density and the chemical potential stays at a fixed value given by the negative of the Silicon work function W_{Si} , i.e.

$$\mu_{\text{Si}} \approx -W_{\text{Si}}. \quad (\text{S32})$$

In BLG the charge density can be expressed as

$$\rho_{\text{BLG}} = -e(n_{\text{BLG}} - \bar{n}_{\text{BLG}}), \quad (\text{S33})$$

where n_{BLG} is the density of mobile carriers that determines the plasmon dispersion and $e\bar{n}_{\text{BLG}}$ is the residual charge density that is left in BLG when the Fermi level is at the Dirac point due to impurity doping. Approximating the first valence and conduction bands of BLG as parabolic bands yields an energy independent density of states in the vicinity of the Dirac point given by $g = 2m^*/(\pi\hbar^2)$ with $m^* \approx 0.046 m_e$, m_e being the bare electron mass. This allows us to calculate n_{BLG} as

$$n_{\text{BLG}} = g [I(\mu_{\text{BLG}} - E_D, k_B T) - I(-\mu_{\text{BLG}} + E_D, k_B T)] = g(\mu_{\text{BLG}} - E_D), \quad (\text{S34})$$

where $E_D \approx -4.5$ eV is the energy of the Dirac point of BLG measured from the vacuum level, and

$$I(\mu, k_B T) = \int_0^\infty \frac{dE}{1 + \exp[(E - \mu)/(k_B T)]} = k_B T \ln \left(1 + e^{\frac{\mu}{k_B T}} \right) \stackrel{\frac{|\mu|}{k_B T} \gg 1}{\approx} \begin{cases} \mu & \mu > 0 \\ k_B T e^{\frac{\mu}{k_B T}} & \mu < 0. \end{cases} \quad (\text{S35})$$

Imposing that BLG is electrically neutral when the chemical potential equals the negative of the work function of isolated BLG \bar{W}_{BLG} (in the following bars will denote quantities related to the isolated materials) we obtain

$$-eg(-\bar{W}_{\text{BLG}} - E_{\text{D}}) + e\bar{n}_{\text{BLG}} = 0, \quad (\text{S36})$$

that we can use to eliminate E_{D} in (S34). Solving for the chemical potential gives

$$\mu_{\text{BLG}} = -\bar{W}_{\text{BLG}} + \frac{e^2}{C_{\text{Q}}}(n_{\text{BLG}} - \bar{n}_{\text{BLG}}), \quad (\text{S37})$$

where $C_{\text{Q}} = e^2g \approx 62 \text{ mF/m}^2$ is the quantum capacitance of BLG.

Similarly, in WSe_2 we can write the charge density as

$$\rho_{\text{WSe}_2} = -e(n_{\text{WSe}_2} - e\bar{n}_{\text{WSe}_2}), \quad (\text{S38})$$

where n_{WSe_2} is the number of mobile carriers in the bands (electrons-holes) and $e\bar{n}_{\text{WSe}_2}$ is a residual charge density due to doping. Again, approximating the relevant bands with an effective mass we get constant densities of states in the conduction and valence bands $g_{\text{C/V}}$ (using values from Eq. S20), and the carrier density can be calculated according to

$$n_{\text{WSe}_2}[\mu_{\text{WSe}_2}] = g_{\text{C}}I(\mu_{\text{WSe}_2} - E_{\text{C}}, k_{\text{B}}T) - g_{\text{V}}I(E_{\text{V}} - \mu_{\text{WSe}_2}, k_{\text{B}}T), \quad (\text{S39})$$

where $E_{\text{C/V}}$ are the edges of the conduction/valence band edges measured from the vacuum level. Imposing charge neutrality when the chemical potential equals minus the work function of isolated WSe_2 gives

$$\bar{n}_{\text{WSe}_2} = g_{\text{C}}I(-\bar{W}_{\text{WSe}_2} - E_{\text{C}}, k_{\text{B}}T) - g_{\text{V}}I(E_{\text{V}} + \bar{W}_{\text{WSe}_2}, k_{\text{B}}T). \quad (\text{S40})$$

In the following we will express the chemical potential of WSe_2 in terms of a deviation $\Delta\bar{\mu}_{\text{WSe}_2}$ from its value in pristine WSe_2 , i.e.

$$\mu_{\text{WSe}_2} = -\bar{W}_{\text{WSe}_2} + \Delta\bar{\mu}_{\text{WSe}_2}. \quad (\text{S41})$$

C. Equilibrium of electrochemical potential

The voltage source connected at the bottom gate fixes the electrochemical potential difference between BLG and silicon to be

$$\Phi_{\text{Si}} - \Phi_{\text{BLG}} = V_{\text{B}}, \quad (\text{S42})$$

substituting (S30-S32-S28-S37) we can solve for the silicon surface charge density

$$\rho_{\text{Si}} = C_{\text{B}} \left(V_{\text{B}} - \bar{V}_{\text{B}} - e \frac{n_{\text{BLG}} - \bar{n}_{\text{BLG}}}{C_{\text{Q}}} \right), \quad (\text{S43})$$

where $\bar{V}_{\text{B}} = (W_{\text{Si}} - \bar{W}_{\text{BLG}})/e$.

In a similar way we can write for the top-gate voltage

$$\Phi_{\text{WSe}_2} - \Phi_{\text{BLG}} = V_{\text{T}}, \quad (\text{S44})$$

and, substituting (S27-S41-S28-S37), solve for the WSe_2 charge density

$$\rho_{\text{WSe}_2} = C_{\text{T}} \left(V_{\text{T}} - \bar{V}_{\text{T}} + \frac{\Delta\bar{\mu}_{\text{WSe}_2}}{e} - e \frac{n_{\text{BLG}} - \bar{n}_{\text{BLG}}}{C_{\text{Q}}} \right). \quad (\text{S45})$$

Here, $\bar{V}_{\text{T}} = (\bar{W}_{\text{WSe}_2} - \bar{W}_{\text{BLG}})/e$.

Substituting (S33-S43-S45) into the charge neutrality condition (S25) gives

$$\left(1 + \frac{C_{\text{T}}}{C_{\text{Q}}} + \frac{C_{\text{B}}}{C_{\text{Q}}} \right) e(n_{\text{BLG}} - \bar{n}_{\text{BLG}}) = C_{\text{T}}(V_{\text{T}} - \bar{V}_{\text{T}}) + C_{\text{B}}(V_{\text{B}} - \bar{V}_{\text{B}}) + \frac{C_{\text{T}}}{e} \Delta\bar{\mu}_{\text{WSe}_2}, \quad (\text{S46})$$

that, together with the equation obtained by eliminating ρ_{WSe_2} from (S38) and (S45),

$$-en_{\text{WSe}_2}[-\bar{W}_{\text{WSe}_2} + \Delta\bar{\mu}_{\text{WSe}_2}] + e\bar{n}_{\text{WSe}_2} = C_{\text{T}} \left(V_{\text{T}} - \bar{V}_{\text{T}} + \frac{\Delta\bar{\mu}_{\text{WSe}_2}}{e} - e \frac{n_{\text{BLG}} - \bar{n}_{\text{BLG}}}{C_{\text{Q}}} \right), \quad (\text{S47})$$

constitutes a system of two non-linear equations in the two variables n_{BLG} and $\Delta\bar{\mu}_{\text{WSe}_2}$ that can be solved numerically.

However, before solving these equations we exploit the fact that $C_Q \gg C_T, C_B$ and take the limit $C_Q \rightarrow \infty$. This gives

$$e(n_{\text{BLG}} - \bar{n}_{\text{BLG}}) = C_T(V_T - \bar{V}_T) + C_B(V_B - \bar{V}_B) + \frac{C_T}{e}\Delta\bar{\mu}_{\text{WSe}_2}, \quad (\text{S48})$$

$$-en_{\text{WSe}_2}[-\bar{W}_{\text{WSe}_2} + \Delta\bar{\mu}_{\text{WSe}_2}] + e\bar{n}_{\text{WSe}_2} = C_T\left(V_T - \bar{V}_T + \frac{\Delta\bar{\mu}_{\text{WSe}_2}}{e}\right). \quad (\text{S49})$$

Note that in this approximation the second equation (S49) does not depend on V_B .

To simplify the analysis of experimental results it is useful to use as a reference in our equations the zero bias situation ($V_B = V_T = 0$) instead of the flat vacuum level situation ($V_B = \bar{V}_B, V_T = \bar{V}_T$). This can be done by defining $\Delta\bar{\mu}_{\text{WSe}_2}^0$ as the solution of

$$-en_{\text{WSe}_2}[-\bar{W}_{\text{WSe}_2} + \Delta\bar{\mu}_{\text{WSe}_2}^0] + e\bar{n}_{\text{WSe}_2} = C_T\left(-\bar{V}_T + \frac{\Delta\bar{\mu}_{\text{WSe}_2}^0}{e}\right). \quad (\text{S50})$$

Subtracting (S50) from (S49), and defining $W_{\text{WSe}_2}^0 = \bar{W}_{\text{WSe}_2} - \Delta\bar{\mu}_{\text{WSe}_2}^0$, and $\Delta\mu_{\text{WSe}_2} = \Delta\bar{\mu}_{\text{WSe}_2} - \Delta\bar{\mu}_{\text{WSe}_2}^0$, gives our final equation for the chemical potential shift $\Delta\mu_{\text{WSe}_2}$

$$\boxed{n_{\text{WSe}_2}[\Delta\mu_{\text{WSe}_2} - W_{\text{WSe}_2}^0] - n_{\text{WSe}_2}[-W_{\text{WSe}_2}^0] = -\frac{C_T}{e}\left(V_T + \frac{\Delta\mu_{\text{WSe}_2}}{e}\right)}. \quad (\text{S51})$$

The result can be then fed into

$$\boxed{n_{\text{BLG}} = \frac{C_B(V_B - V_D)}{e} + \frac{C_T V_T}{e} + \frac{C_T \Delta\mu_{\text{WSe}_2}[V_T]}{e^2}}, \quad (\text{S52})$$

that is derived from (S48) by defining $n_{\text{BLG}}^0 = \bar{n}_{\text{BLG}} - C_B \bar{V}_B/e - C_T \bar{V}_T/e + C_T \Delta\bar{\mu}_{\text{WSe}_2}^0/e^2$, $V_D = -en_{\text{BLG}}^0/C_B$. Note that $\Delta\mu_{\text{WSe}_2}[V_T = 0] = 0$.

D. Solution of Eqs. (S51-S52)

To solve Eq. (S51) for $\Delta\mu_{\text{WSe}_2}$ as a function of V_T requires in general the use of a numerical root finding method. However, it is instructive to look at the zero temperature limit where an analytical solution can be derived. Making use of (S35) the left hand side of (S51) simplifies, at zero temperature, to

$$n_{\text{WSe}_2}[\Delta\mu_{\text{WSe}_2} - W_{\text{WSe}_2}^0] - n_{\text{WSe}_2}[-W_{\text{WSe}_2}^0] = \begin{cases} g_V(\Delta\mu_{\text{WSe}_2} + eV_V) & \Delta\mu_{\text{WSe}_2} < -eV_V \\ 0 & -eV_V \leq \Delta\mu_{\text{WSe}_2} \leq -eV_C \\ g_C(\Delta\mu_{\text{WSe}_2} + eV_C) & \Delta\mu_{\text{WSe}_2} > -eV_C, \end{cases} \quad (\text{S53})$$

where $V_C = -(E_C + W_{\text{WSe}_2}^0)/e$ and $V_V = -(E_V + W_{\text{WSe}_2}^0)/e$.

This expression is plotted in Figure (S4) as dashed line together with the right-hand side of (S51) calculated for three different values of V_T . The solution can be obtained by the intersection of the two curves and gives, in the zero temperature limit, a piecewise linear function

$$\Delta\mu_{\text{WSe}_2}[V_T] = \begin{cases} \frac{-eV_C - eV_T \frac{C_T}{e^2 g_C}}{1 + \frac{C_T}{e^2 g_C}} \approx -eV_C & V_T < V_C \\ -eV_T & V_C \leq V_T \leq V_V \\ \frac{-eV_V - eV_T \frac{C_T}{e^2 g_V}}{1 + \frac{C_T}{e^2 g_V}} \approx -eV_V & V_T > V_V, \end{cases} \quad (\text{S54})$$

where we made use of $e^2 g_{C,V} \gg C_T$. Figure (S4) also shows the finite-temperature curve showing that at finite temperature solution is always closer to zero than the zero-temperature one. We can then compare the full numerical result with the analytical, zero-temperature approximation. These are shown in Figure (S5). We see that the numerical and the analytical solutions agree qualitatively, showing a linear behavior for values of the top-gate voltage inside the WSe_2 gap and saturations at the conduction and valence band edges. However, finite temperature effects significantly reduces the value of $\Delta\mu_{\text{WSe}_2}$. From (S52) we can calculate the shift in density produced by the application of V_T , again, in the zero temperature limit,

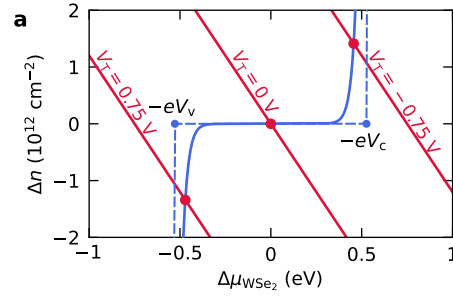


Fig. S4 | Graphical solution of Eq. (S51). The tick blue curve represents the left hand side of (S51) evaluated at room temperature $k_B T = 0.026\text{eV}$. The thin red lines represent the the right hand side of (S51) for three different values of V_T . The dashed blue curve represents the left hand side of (S51) evaluated at zero temperature.

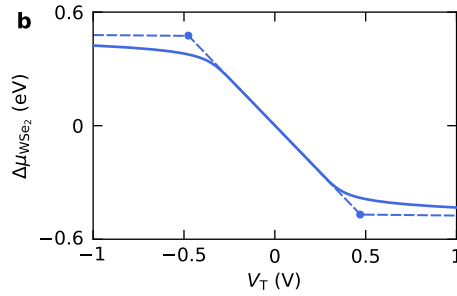


Fig. S5 | Solution of Eq. (S51). The thick blue line represents $\Delta\mu_{\text{WSe}_2}$ as a function of V_T calculated by solving numerically (S51). The blue dashed line represents the zero-temperature solution (S54).

this gives

$$\delta n_{\text{BLG}} = n_{\text{BLG}} - n_{\text{BLG}}^0 - \frac{C_B V_B}{e} = \frac{C_T}{e} \times \begin{cases} V_T - V_C & V_T < V_C \\ 0 & V_C \leq V_T \leq V_V \\ V_T - V_V & V_T > V_V. \end{cases} \quad (\text{S55})$$

And we compare the analytical solution with the full numerical solution and experimental data in Figure (S6).

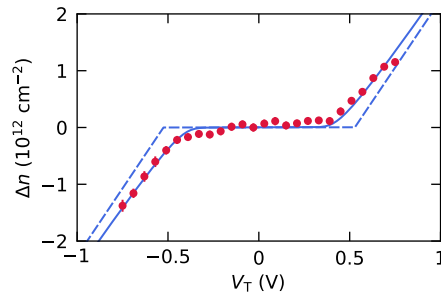


Fig. S6 | Carrier density induced by the application of a top-gate voltage. Dots are experimental data, the thick blue curve is the full numerical solution while the dashed blue curve corresponds to the analytical zero-temperature solution.

SUPPLEMENTARY REFERENCES

- [S1] Gjerding, M. et al. Atomic simulation recipes: A python framework and library for automated workflows. *Computational Materials Science* **199**, 110731 (2021).
- [S2] Enkovaara, J. et al. Electronic structure calculations with gpaw: a real-space implementation of the projector augmented-wave method. *Journal of physics: Condensed matter* **22**, 253202 (2010).
- [S3] Hastrup, S. et al. The computational 2d materials database: high-throughput modeling and discovery of atomically thin crystals. *2D Materials* **5**, 042002 (2018).

- [S4] Gjerding, M. N. et al. Recent progress of the computational 2d materials database (c2db). *2D Materials* **8**, 044002 (2021).
- [S5] Grimme, S., Antony, J., Ehrlich, S. & Krieg, H. A consistent and accurate ab initio parametrization of density functional dispersion correction (dft-d) for the 94 elements h-pu. *The Journal of chemical physics* **132**, 154104 (2010).